International Journal of Computer Assisted Radiology and Surgery
https://doi.org/10.1007/s11548-026-03615-1

ORIGINAL ARTICLE

Intraoperative fusion of models and data for robust distance sensing

Marius Briel[1,2] · Ludwig Haide[1] · Tobias Weber[3] · Alain Jungo[4] · Nicola Piccinelli[5] · Gernot Kronreif[6] · Franziska Mathis-Ullrich[2] · Eleonora Tagliabue[1]

Received: 31 August 2025 / Accepted: 6 January 2026

Abstract

Purpose Instrument-integrated optical sensors are gaining popularity in microsurgery due to their ability to provide accurate measurements of instrument-to-tissue distances, enabling precise instrument control. However, obstructions in the optical path can result in measurement errors. In this work, we propose a method to improve robustness of distance information from sensorized microsurgical instruments.

Methods Our pipeline integrates a rapid search algorithm to identify relevant neighboring data points, as well as geometric and non-geometric techniques to accurately model the local tissue structure. Additionally, we implement a fusion of measurement and model to identify and overcome disturbances, e.g., obstructions from surgical instruments or semantic segmentation errors.

Results Our simulation examines the effect of different modeling parameters and techniques on distance prediction, yielding a mean absolute error of less than 0.02 mm when using the local spline fit. Experiments in ex vivo human eyes show that our pipeline achieves up to 89 % error reduction when compared to sensor only.

Conclusion Our method improves the reliability of instrument-integrated optical sensors. This work could enable distance-based instrument control in challenging conditions, thereby enhancing surgical precision in delicate ophthalmic procedures. Our approach can be generalized to any surgery with sensorized instruments and beyond.

Keywords Microsurgery · Sensorized instruments · Optical coherence tomography · Geometric modeling

Introduction

Microsurgery involves the manipulation of delicate anatomical structures, often at sub-micrometer scales. Precise control of surgical instruments requires thorough understanding of instrument-to-tissue distances. Currently, surgical microscopes are predominantly used for their magnified visualization; however, depth perception remains challenging [1]. Recently, sensorized surgical instruments, such as endoscopes [2] or instrument-integrated optical coherence tomography (iiOCT) iiOCT probes [3, 4], are gaining popularity as they allow for internal imaging, thereby increasing the precision of instrument manipulation. The fiber-based implementation of optical coherence tomography (OCT) acquires A-scans that extend outward from the fiber tip to measure fiber-to-tissue distances. Fiber-based oct distance sensing has been validated for assistance in three surgical tasks [5] and has undergone in vivo clinical validation [6, 7]. In previous work, we developed a controller that maintains a specified instrument-to-retina distance. This system is complemented by haptic shared control, which assists ophthalmic surgeons during endolaser photocoagulation procedures [8]. However, obstructions in the optical path can result in wrong distance measurements, as demonstrated in porcine eye experiments. In such cases, the distances to these objects can be determined, but the distances to the tissue remain unknown, complicating distance control.

✉ Marius Briel
marius.briel@zeiss.com

1 Carl Zeiss AG, Oberkochen, Germany

2 Laboratory for Surgical Planning and Robotic Cognition (SPARC), Friedrich-Alexander-University, Erlangen, Germany

3 Karlsruhe Institute of Technology, Karlsruhe, Germany

4 ARTORG Center, Universität Bern, Bern, Switzerland

5 Department of Engineering for Innovation Medicine, Università di Verona, Verona, Italy

6 Austrian Center for Medical Innovation and Technology, Wiener Neustadt, Austria

Published online: 08 May 2026

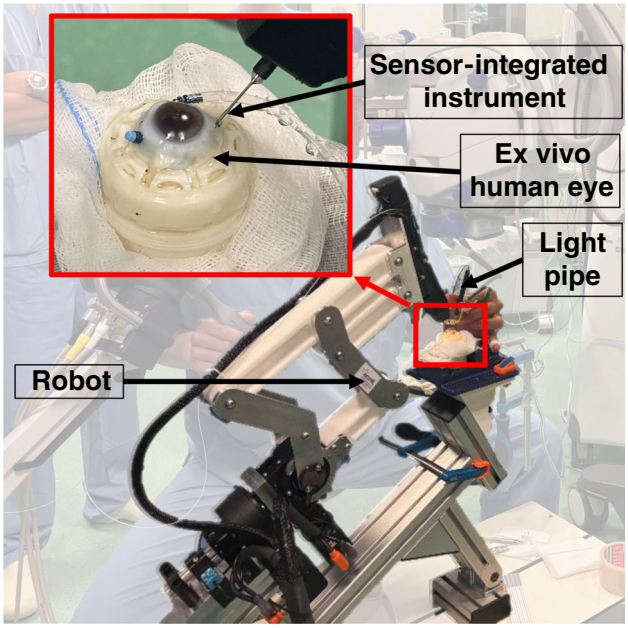

Fig. 1 Experimental setup featuring the GEYEDANCE robot holding a cannula with an integrated optical fiber, inserted into an ex vivo human eye

Vitreoretinal surgery is a crucial area of microsurgery that involves procedures within the vitreous body, a gel-like substance in the eye's posterior segment (Fig. 1). To facilitate instrument-to-retina distance estimations during vitreoretinal surgery, optical fibers have been integrated into forceps [9], vitrectomy cutters [10], and endolaser probes [11]. In retinal surgery, occluding objects can consist of peeled membranes suspended in the vitreous, vitreous floaters, blood [12], dyes [13, 14], surgical tools such as light pipes [15], and fragments of dropped nucleus [16], varying according to the specific procedure being performed. During cataract surgery, the eye lens may descend as a result of a rupture in the posterior lens capsule, necessitating an immediate vitrectomy.

Accurately estimating distances from iiOCT scans necessitates a segmentation algorithm to identify the pixel in the A-scan image corresponding to the distance to the outermost layer (Fig. 2a). Lee et al. utilize a U-Net to extract retinal layers from A-scans and apply a Kalman filter to enhance performance in dynamic settings [17]. Segmentation failures can arise from artifacts in iiOCT, which include speckle noise, intensity decay, or patient-related motion artifacts such as blurring [18]. Additionally, polarization settings in dual-arm fiber-based systems must be carefully adjusted, as incorrect settings can attenuate the signal [19]. A linear artifact can occur due to defects in the optical fiber. The segmentation algorithm may misinterpret these artifacts, leading to inaccurate distance estimations (Fig. 2b).

When employing a deep learning-based approach, irregularities not included in the training data can lead to erroneous

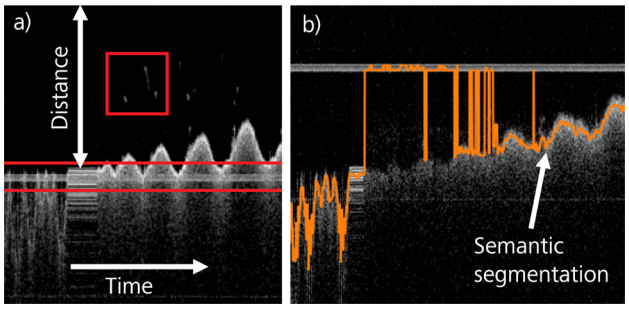

Fig. 2 Examples of OCT-related artifacts, such as (**a**) speckle noise (red square) and a constant artifact (red rectangle), as well as (**b**) erroneous segmentation (orange line) caused by the artifacts and an intensity decrease as the instrument-to-tissue distance increases. The images were acquired using an IOL Master 700 OCT engine (Zeiss, Germany), as described in our previous work [20]

algorithm behavior. For instance, if the training data set lacks images of retinal detachments, segmentation failures may occur in those cases.

Endolaser photocoagulation involves delivering laser energy through an endoprobe positioned close to the retina. Maintaining a consistent instrument-to-retina distance of approximately 2 mm to 3 mm throughout the procedure is crucial for controlling the size and energy density of each laser spot [21]. To ensure uniform lesions, the permissible distance deviation is approximately $\pm 500\,\mu$m [8]. Excessive energy deposition can cause irreversible retinal damage, while insufficient energy may fail to achieve the desired therapeutic effect.

In this work, we propose a novel processing pipeline that utilizes two sources for estimating instrument-to-retina distance, enhancing the robustness of distance control during endolaser photocoagulation. A key component of this pipeline is the local geometric model, which is employed when a measurement is not consistent. We are testing this approach on human cadaver eyes, but it is also applicable to other microsurgery scenarios and beyond.

Method

Our pipeline is divided into two horizontal levels: signal level and feature level (Fig. 3). The signal level inputs A-scans and instrument poses to our pipeline, while the feature level corresponds to distance measurements. When an A-scan enters the pipeline, semantic segmentation estimates a distance d_{sensor}. Concurrently, an alternative distance d_{model} is derived from the retinal model and the pose of the surgical instrument, obtained through instrument tracking or robot kinematics, similarly to [22]. Both estimates are checked for consistency at the distance level to determine the output dis-

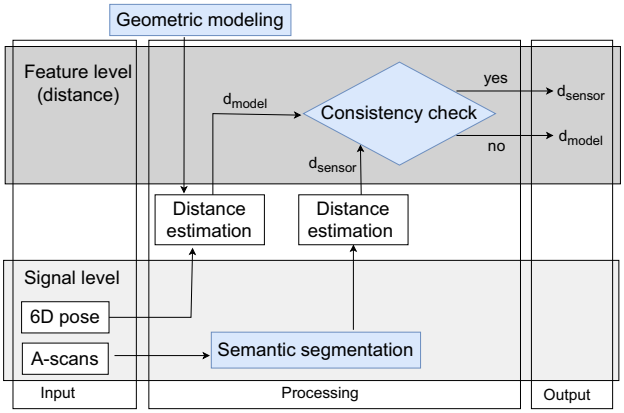

Fig. 3 Pipeline for robust instrument-to-retina distance estimation using OCT sensing and local geometric modeling

tance d. In the following, the different components of the pipeline are explained.

Semantic segmentation

A one-dimensional U-Net-like convolutional neural network is employed to predict the distance to the retina from individual A-scans. The network outputs a probability vector of the same size, assigning a probability of being the retinal boundary to each pixel. The pixel with the highest probability is identified as the boundary pixel. The physical distance is then calculated by multiplying the pixel distance by the axial pixel resolution. Our 1D U-Net consists of eight depth levels, each containing two convolutional layers. A distinguishing feature of the U-Net architecture is its shape and the skip connections that link layers at the same depth level. These connections enable the network to focus on finer-grained local features in the A-scan while also capturing global, coarser features from the deeper layers.

The network is trained by optimizing the cross-entropy loss between the target and predicted probability vectors. The target vectors are set to one at the pixel representing the retinal boundary and zero elsewhere. In cases where the anatomical structure of interest is beyond the scan range, the target vector is assigned a uniform distribution. We train the neural network for 25 epochs with a batch size of 16, using Adam optimizer with a learning rate of 10^{-4}. Neural network selection is based on performance on the validation set with respect to cross-entropy.

For the specific use case considered in this paper, the network was trained on A-scans that were recorded during a previous preclinical trial (see Section Cadaver eye experiments). The retinal boundary was manually annotated for a subset of the data, resulting in a data set comprising 34,316 A-scans (12,736 for training, 6000 for validation, and 15,580 for testing).

The trained neural network achieves a mean absolute distance error of 3.26 pixels on the test data set, excluding artifacts, with an average computation time of 2.57 ms and maximum computation time of 3.65 ms over 100 runs on the CPU. The pixel count corresponds to a mean error of 7 µm.

Geometric modeling

Our pipeline incorporates a rapid search algorithm to identify relevant retinal points within a local search cylinder (LSC) surrounding the instrument axis from a pre-recorded retinal data set (RDS). We assume that such a pre-recorded data set is available and can be used to create the intraoperative models. The data set needs to cover the entire area of surgical interest with sufficient density and could be acquired during previous surgical steps or preoperatively. Both geometric and non-geometric techniques are then employed to accurately model the local retinal structure based on the points found in the LSC. When neighboring points are not available, a global model is employed to extrapolate beyond the available data points. Previously, eyes have been modeled as spheres [22], ellipsoids [20], or with the help of more flexible radial basis functions [23]. However, these models have not been utilized to improve intraocular distance estimation.

Local search cylinder

First, we identify pre-recorded retinal points that do not exceed a specified distance from the current iiOCT ray (Fig. 4a). If the ray's direction aligns with the z-axis of a coordinate system (after transforming the retinal data points), the range is calculated as $r = \sqrt{x^2 + y^2}$. Ultimately, r is compared to the specified radius r_{LSC} of the LSC for each pre-recorded retinal data point.

Local model

Geometric models, such as sphere or plane fits, aim to approximate the geometric shape of the retina. We implemented a local plane fit using singular value decomposition, and a bivariate B-spline fitting approach, allowing for curvature in the surface model. Using the geometric model, an estimate of the distance to the retina can be determined from the intersection between the iiOCT ray direction and the model (Fig. 4b). Conversely, non-geometric models, such as closest point or average, directly calculate the model estimate from the RDS points within the LSC. The closest point is identified using nearest neighbor search, and the average is computed by taking the componentwise average of the points within the LSC. For the weighted average, the weight is defined as the inverse of the range r between a point in the LSC and the iiOCT ray. This approach reduces the influence of points that are farther from the ray.

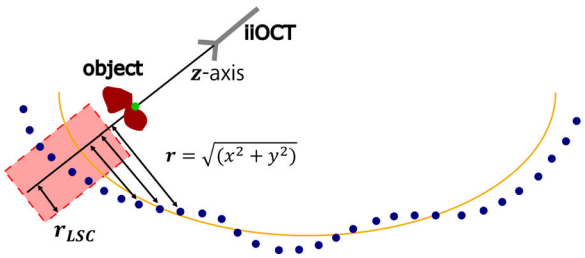

(a) An object positioned between the sensor and the retina obstructs the optical path, causing the measured point to be located on the object instead of the retina

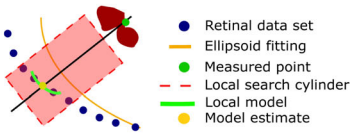

(b) The proposed method utilizes a previously recorded retinal data set to identify points near the ray. A local model is constructed from these points, enabling accurate distance estimation

Fig. 4 Our local modeling approach identifies and models points near the iiOCT ray to address and compensate inconsistent distance measurements

Global model

If there are not enough points in the LSC, the local model cannot be built. In such a case, a spherical model [20] is constructed to extrapolate beyond the measured retinal area.

Consistency check

Anomalous iiOCT A-scans can be detected prior to semantic segmentation. Jungo et al. propose an unsupervised out-of-distribution detection approach that does not require anomalous data for training [24]. However, we propose to identify inconsistent measurements at the distance level after semantic segmentation. The consistency check is conducted to identify measurement failures using the absolute difference Δd between the model estimate d_{model} and the measured value d_{sensor}. A distance anomaly is identified when the absolute difference Δd exceeds a specified threshold τ, which serves to adjust the sensitivity of the consistency check (Algorithm 1).

Algorithm 1 Consistency check and fusion

Input: d_{sensor}, $d_{\text{model(local)}}$, $d_{\text{model(global)}}$
Output: d
if $|\text{LSC}| \geq N$ **then**
  if $\Delta d = |\, d_{\text{sensor}} - d_{\text{model(local)}} \,| \leq \tau_l$ **then**
    $d = d_{\text{sensor}}$
  else
    $d = d_{\text{model(local)}}$
  end if
else
  if $\Delta d = |\, d_{\text{sensor}} - d_{\text{model(global)}} \,| \leq \tau_g$ **then**
    $d = d_{\text{sensor}}$
  else
    $d = d_{\text{model(global)}}$
  end if
end if
return d

The thresholds are determined empirically, set at $\tau_l = 0.6$ mm for the local model and $\tau_g = 1.2$ mm for the global model. Setting τ as small as possible but larger than the model inaccuracy is the rationale behind this choice. The higher threshold for the global model reflects its lower accuracy. If τ is set too large, smaller deviations may go undetected; if set too small, valid values may be mistakenly discarded.

Experimental validation

We test the presented pipeline in both simulation and real-world experiments. In simulation, we consider a point cloud of the eye with a pointed posterior that mimics a pathologic myopic eye shape, as introduced in [20]. Simulation allows a thorough evaluation of the pipeline since the ground truth eye shape is available, enabling accurate simulated distance measurements. Real-world tests are performed during a preclinical study on cadaver eyes. Due to the lack of ground truth eye shape, the pipeline output is compared to a previously recorded reference trajectory, limiting the evaluation accuracy to the order of the system repeatability.

Simulation experiments

We developed a Python-based simulation, which incorporates a designed pointed eye shape and the surgical instrument defined by the remote center of motion (RCM) and the instrument tip. As the tip of the instrument is moved inside the eye, simulated measurements are taken by casting a beam from the tip of the instrument in the direction of the instrument to the shape of the eye.

Figure 5 shows the RDS that includes the intersection points that are created by moving the instrument tip along an Archimedean spiral (Fig. 6).

To mimic the imperfections of iiOCT measurements, Gaussian noise with a standard deviation of 20 µm is artificially added in the axial direction. For our simulation experiments, we assume that all measurements along the trajectory are erroneous due to an occluding object, so the model estimate must be used at all times. To fit the geometric models and compute the non-geometric model predictions, the RDS points inside the cylinder are used.

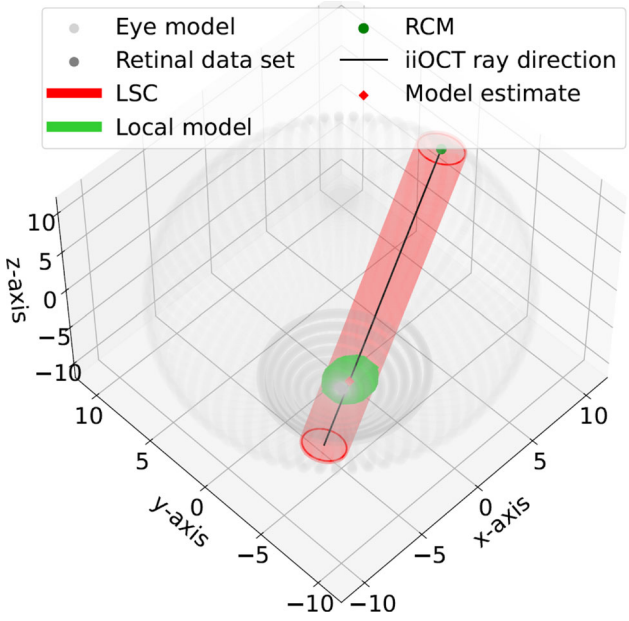

Fig. 5 Simulation environment comprising an eye shape and a surgical instrument that pivots on an eye insertion point

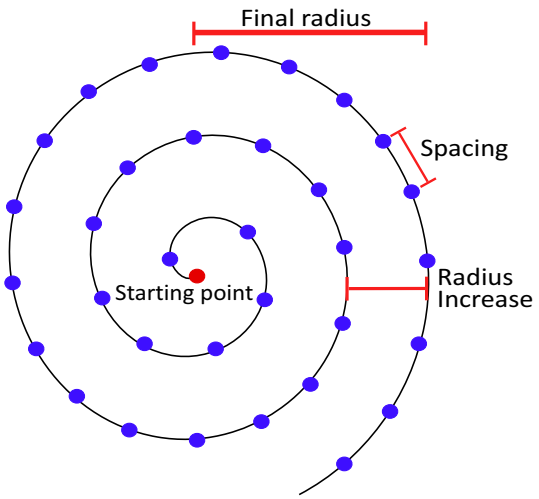

Fig. 6 Archimedean spiral used as the rds, with sampling points depicted in blue. Spacing and radius increase define the point density

We leverage on the simulation experiments to identify optimal parameters, such as the spacing and radius increase of the spiral, and the size of the LSC. It is key to find parameters that meet the accuracy requirements of an intraoperative distance sensor while not unnecessarily prolonging the duration of the surgical procedure. In addition to proving the feasibility of the pipeline concept, suitable modeling approaches, that are used in the real-world experiments, are determined in simulation. Euclidean distances $||\mathbf{p}-\mathbf{p}_{\text{ref}}||$ between model estimates $\mathbf{p}$ and its closest ground truth retinal point $\mathbf{p}_{\text{ref}}$ serve as an error measure.

Cadaver eye experiments

Preclinical studies were conducted to demonstrate the transferability from simulation to a real-world scenario. The preclinical tests were conducted at the Ospedale Privato Villa Igea in Forlì, Italy, as part of the GEYEDANCE project [25]. Two ex vivo human eyes were prepared (i.e., lens removal and vitrectomy) by two retinal surgeons. The inner limiting membrane (ILM) required removal due to its complete detachment. Three trocars were placed for the light pipe, the surgical instrument (including the iiOCT sensor) and the irrigation cannula. The movements of the surgical instruments were executed by a robotic manipulator, while the light pipe was maneuvered manually by the surgeon (Fig. 1). An eye holder provided by the Veneto Eye Bank was used for eye fixation.

The GEYEDANCE distance sensing module [25] employs a common-path spectral domain oct with an imaging depth of 12.8 mm in air, using the tip of the measurement fiber as the interferometer's zero-delay position. A gradient index fiber (GRIF) is fusion-spliced to the end of the single-mode fiber, serving as a focusing lens. The fiber optic is part of a microsurgical cannula. The GEYEDANCE robotic manipulator, used for instrument positioning and tracking, features three degrees of freedom (DOF) due to its parallelogram structure, which establishes a hardware-defined RCM. Precise knowledge of the iiOCT pose relative to the robot is essential for reconstructing retinal points from iiOCT measurements. To accurately estimate such a transformation, we adapt the calibration procedure proposed by Sifferman et al. [20, 26].

Our method requires pre-surgery data acquisition of the RDS to create the models, allowing it to function independently of potentially erroneous online measurements. An Archimedean spiral (Fig. 6) with a radius increase of 0.5 mm, a spacing of approximately 20 µm between scan points, and a radius r_{LSC} of 1.5 mm is used. These parameters were found to be optimal from simulation experiments. The RDS should encompass the area where surgery is performed to enable fitting of local models. For macula edema treatment using photocoagulation, given that the macula can be up to 6 mm wide, the final diameter of the spiral is set to 8 mm. In addition to the spiral, a 10 mm $\times$ 10 mm grid with a spacing of 40 µm is recorded as an alternative RDS. The RDS grid allows us to benchmark our spiral retinal data set, as the grid is extremely dense and allows for accurate modeling. However, the grid scan is very time consuming, making its use in clinical settings undesirable.

Subsequently, an occlusion-free trajectory $\{d_{\text{ref}}\}$ is recorded to serve as a reference, mimicking the movements of real retinal surgery. Next, an identical trajectory $\{d_{\text{sensor}}\}$ is recorded with occlusions, starting from the same position to ensure comparability with the reference. In this preclinical study, two types of occlusions were tested. On the first

Table 1 Duration to acquire the RDS spiral

Radius increase [mm]	0.1	0.2	0.4	0.5	1.0
Time t_s [s]	254	128	65	53	27

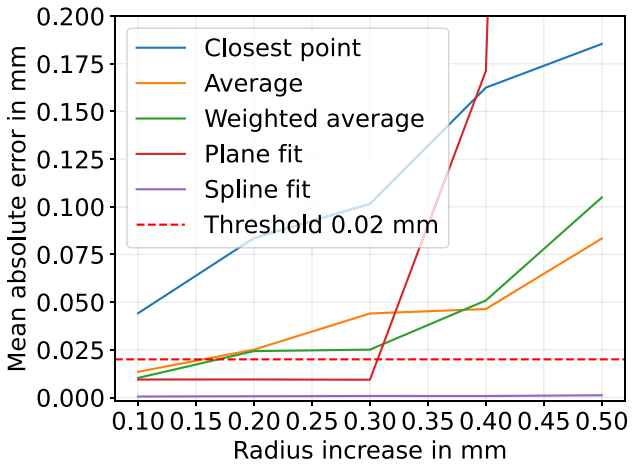

Fig. 7 Simulation results: comparison of different local modeling approaches used within our distance estimation pipeline. The red dotted line indicates the desired distance prediction accuracy of 20 µm

eye, the surgeon inserted the light pipe at irregular intervals, obstructing the sensor's view of the retina. On the second eye, the dropped eye lens was placed on the retina while executing the trajectory.

The data from the trajectories with occlusions are fed into the pipeline, and the pipeline output $\{d\}$ is compared with the reference trajectory $\{d_{\text{ref}}\}$. The mean absolute error (MAE) averages the absolute differences $|\, d - d_{\text{ref}} \,|$ along the trajectories. Additionally, the consistency check is evaluated using percentages of true positives, true negatives, false positives, and false negatives. We define a distance measurement as *irregular* when it deviates more than 0.3 mm from the reference distance. The consistency check is designed to identify such irregular measurements by detecting inconsistencies with the model.

Results

Simulation results

Table 1 lists the RDS acquisition times for different choices of radius increase, with an instrument speed of $v_{max} = 2\,\frac{mm}{s}$. According to retinal surgeons, the time to record the RDS should be below 1 min, necessitating a minimum radius increase of 0.5 mm. With such a sparse spiral, a desired distance prediction error below 20 µm can only be achieved using a spline fitting approach (Fig. 7), justifying the use of spline fits in our real-world experiments.

The plane fit ranks second for a maximum radius increase of 0.3 mm but becomes unstable for larger radius increases. The average and weighted average models exhibit similar errors, while the closest point model shows the highest MAE.

To facilitate real-time model-based distance estimation, the runtime must be faster than 100 Hz. A spacing of 20 µm and a radius increase of 0.5 mm results in 5028 points in the RDS. The runtime on the CPU (*Dell* Latitude 5320 laptop, Intel Core i5-1145G7 CPU) for the coordinate transformation and radius calculation is in the microsecond range, while the less than or equal check requires 1.4 ms. With an LSC radius of 1.5 mm, there are a maximum of 402 points in the LSC, requiring 104 µs for the local spline fit. Therefore, the total computation time, including the neural network's distance inference, is 4.1 ms, satisfying the real-time capability of 100 Hz.

Real-world results

Fig. 8a shows the measured coordinates of the reference trajectory, the RDS, the transition points between models, and the starting point of the trajectory. It is observed that the transition points lie outside the RDS because the LSC extends into the data set, providing sufficient points to fit a spline. In addition, the corresponding measured distances are shown, with dashed vertical red lines indicating the transitions. At the bottom, the pipeline error is illustrated, with absolute error values from the local and global models highlighted in red and azure blue, respectively. A white background indicates that the pipeline output is based on the sensor measurement. The MAE of the pipeline is 0.250 mm with a standard deviation (SD) of 0.337 mm, while the MAE of the measurement is 1.108 mm with a SD of 1.519 mm. 25 % of the pipeline output results from the local spline model, 13 % from the global model and 62 % from the measurement.

Figure 8b is similarly structured to Fig. 8a, but uses a grid as the RDS instead of a spiral. The grid encompasses a larger portion of the trajectory compared to the spiral. Notably, none of the pipeline outputs originates from the global model, as a local model estimate based on the larger grid is always available when the light pipe obstructs the view.

Table 2 presents the MAE and SD of the different pipeline components, along with the sensor measurements not
enhanced by the local model for the tested occlusions.

While the error reduction of 77.4 % in the light pipe experiment is considerable, the error reduction of 21.6 % in the lens experiment is only modest.

The results of the consistency check, linking predicted inconsistencies with actual irregular distance measurements, are presented in Table 3. A discrepancy between sensor-based and model-based distances suggests an inconsistency, whereas a deviation of the sensor-based distance from the

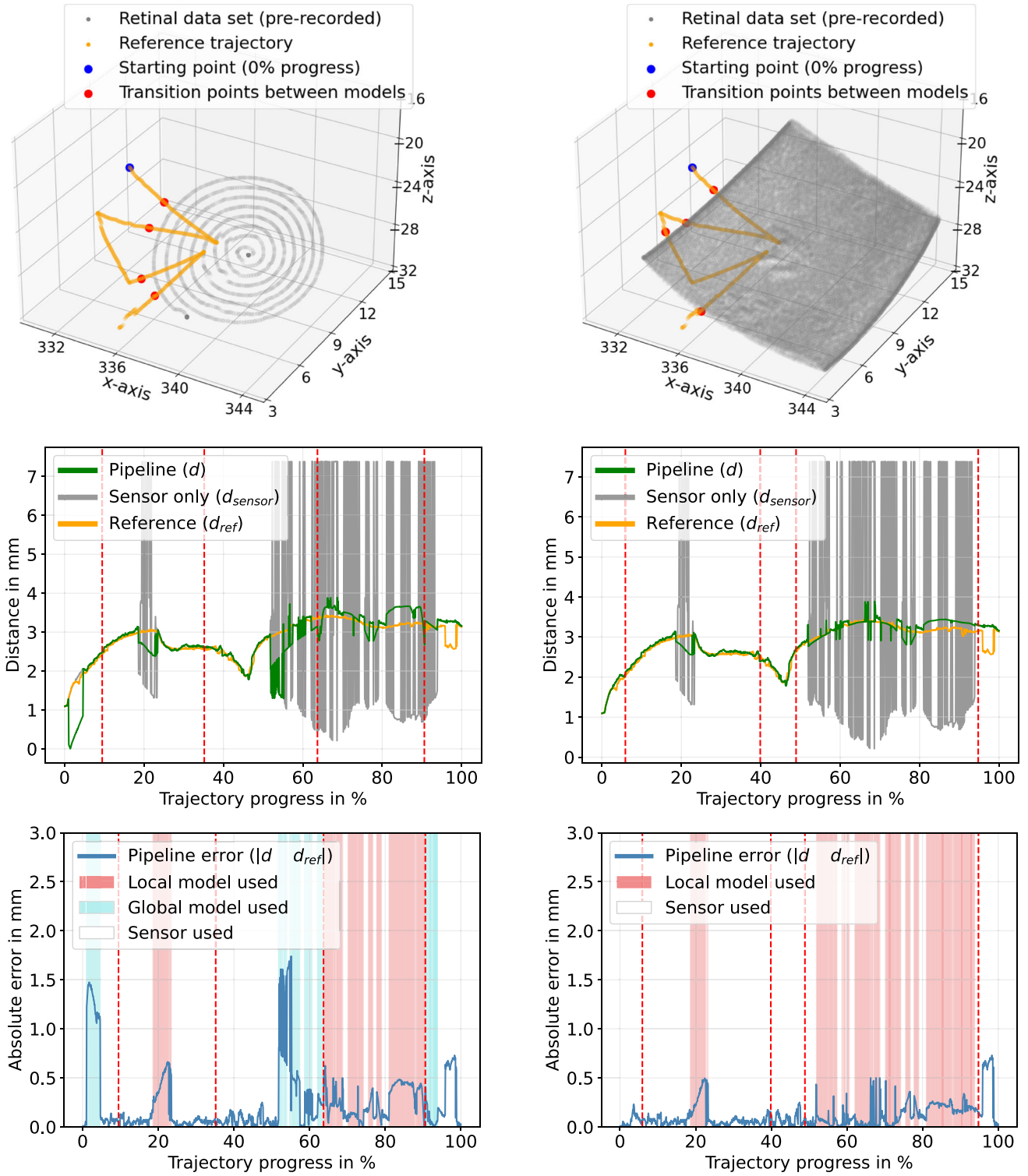

(a) Spiral RDS

(b) Grid RDS

Fig. 8 Real-world results: Data from the light pipe experiment, along with the output from our distance estimation pipeline and the associated error. The plots in the first row visualize the overlap between the trajectories and the rdss. The gray curve (in the second row) represents the neural network's distance estimation with a light pipe occlusion, while the green line shows our pipeline's output, and the orange line shows the reference trajectory. In the error plot (in the third row), the background color indicates whether the local model, the global model or the sensor was used

Table 2 Errors (MAE and SD) of the pipeline and its components compared to the sensor-only measurements (U-Net-based semantic segmentation), for different occlusions and rdss

	Light pipe (spiral)		Light pipe (grid)		Crystalline lens (spiral)	
	MAE [mm]	SD [mm]	MAE [mm]	SD [mm]	MAE [mm]	SD [mm]
Sensor only	1.108	1.519	1.108	1.519	0.680	1.175
Pipeline	**0.250**	**0.337**	**0.117**	**0.134**	**0.533**	**0.648**
Local model used	0.322	0.161	0.146	0.120	0.059	0.054
Global model used	0.590	0.477	–	–	1.311	0.629
Sensor used	0.150	0.300	0.101	0.138	0.202	0.234
Error reduction	77.4 %	77.8 %	89.4 %	91.1 %	21.6 %	44.9 %

The ratio indicates how often the pipeline chose the sensor, the local model, or the global model

Table 3 Results of the consistency check (where $\Delta d = |d_{\text{sensor}} - d_{\text{model}}| < \tau$ indicates consistency) presented as confusion matrices

	Light pipe (spiral)		Light pipe (grid)		Crystalline lens (spiral)	
	Predicted inconsistency ($\Delta d > \tau$)	Predicted consistency ($\Delta d < \tau$)	Predicted inconsistency ($\Delta d > \tau$)	Predicted consistency ($\Delta d < \tau$)	Predicted inconsistency ($\Delta d > \tau$)	Predicted consistency ($\Delta d < \tau$)
Irregular	**452**	75	**475**	52	**228**	106
	34.3 %	5.7 %	36.0 %	3.9 %	17.3 %	8.0 %
Regular	53	**739**	0	**792**	208	**778**
	4.0 %	56.0 %	0 %	60.0 %	15.8 %	58.9 %

A distance measurement is considered irregular (due to occlusion) if it deviates more than 0.3 mm from the reference distance ($|d_{\text{ref}} - d_{\text{sensor}}| > 0.3$ mm). The use of bold numerals indicates true consistency checks

reference signifies an abnormal measurement. Ideally, these two should significantly overlap, approaching a 100 % accuracy in the consistency check.

The consistency check was successful in 90.3 %, 96.1 %, and 76.2 % of the measurements for the light pipe (spiral), light pipe (grid), and lens (spiral) experiments, respectively. These percentages include predicted inconsistencies that accurately reflect irregular measurements, as well as predicted consistencies that align with regular measurements, corresponding to the bold diagonal entries in Table 3.

Discussion

Within the RDS, the pipeline's fundamental principle proves effective, as evidenced by an error reduction of up to 89 % compared to the U-Net without consistency check. The neural network fails to detect the retina when human tissues, such as the crystalline lens, or surgical instruments are interposed. Enhancing U-Net performance might be achieved by employing multilayer segmentation, as variations in retinal layer thickness within A-scans can aid in distinguishing genuine tissue layers from false reflections. Notably, for the phases where the local model was used in the lens experiment, a distance error below 60 µm is achieved. Therefore, the comparatively modest improvement of 22 % in the lens experiment is attributed to the fact that only a small portion of the trajectory lies within the RDS, necessitating reliance on the inaccurate global model. Moreover, pathologies like macular holes or retinal tears can prevent the retina from being accurately represented as a smooth surface. Although B-splines proved effective in modeling the two ex vivo human eyes in this study, additional samples are necessary to challenge the method with a wider range of geometries.

The consistency check works effectively when the model is accurate, as demonstrated in the light pipe experiment with the grid RDS. However, when the spiral is used, correct measurements are occasionally discarded. To achieve more precise outcomes, an accurate measurement setup is essential, along with preprocessing of the RDS to ensure that no outliers are included. Comparing the accuracy of the grid with that of the spiral reveals that a higher point density results in reduced errors due to more accurate modeling.

A limitation of our method is the requirement to acquire retinal data before the pipeline can be used, which consumes valuable operating room time. Registered preoperative data could serve as the RDS [27]. However, to model dynamic changes of the retina, the RDS must be continuously updated. Factors affecting the precision of in vivo iiOCT-based surface reconstructions include patient head movements and involuntary retinal movements [28]. However, the amplitudes of approximately 10 µm for heartbeat and 20 µm for breathing, as noted by Cereda et al. [7], are unlikely to significantly affect our method. Dynamic models are capable of accommodating predictable quasi-periodic movements [29], while unexpected non-periodic movements can be managed

by tracking with alternative sensors, such as the microscope [30].

In summary, preliminary tests with human eyes have been successfully conducted. Our developed pipeline demonstrates improved robustness in retinal distance estimation; however, there remains potential for increased accuracy through enhanced hardware or refined methodologies. This advancement could enable applications in high-precision tasks, such as membrane peeling. Moreover, this approach has the potential to generalize to any surgery using sensorized instruments, including neurosurgery [6], middle ear diagnostics [31], and cochlear implant surgery [4].

Conclusion

The robustness of instrument-to-tissue distance estimations can be enhanced by developing an accurate model to identify inconsistencies in measurements. When inconsistencies are detected, the model provides an alternative estimate. This preclinical study on cadaver eyes indicates that the proposed method achieves distance accuracies of 250 µm and 117 µm for instrument occlusions, depending on the amount of available pre-surgery data. These results fall below the defined safety requirement for endolaser photocoagulation.

Funding Open Access funding enabled and organized by Projekt DEAL. This work was supported by the European Union's Horizon Europe research and innovation program under grant agreement N° 101070443. GEYEDANCE: AI Guidance for Robot-Assisted Eye Surgery (https://geyedance.eu).

Declarations

Conflict of interest The authors have no conflict of interest to declare that are relevant to the content of this article.

Ethics approval and informed consent Donor eyes unsuitable for corneal transplantation due to poor endothelial cell counts, procured by Fondazione Banca degli Occhi del Veneto Onlus (Venice, Italy), were used for research purposes and validation studies described in this manuscript, in accordance with law 91/99 and after an informed consent form was signed by the donor's next of kin. The experimental procedure was approved by the hospital ethics committee (Prot. 2024-0009).

References

1. Probst T, Maninis K-K, Chhatkuli A, Ourak M, Poorten EV, Gool LV (2018) Automatic tool landmark detection for stereo vision in robot-assisted retinal surgery. IEEE Robot Autom Lett 3(1):612–619. https://doi.org/10.1109/LRA.2017.2778020
2. Ajlan RS, Desai AA, Mainster MA (2019) Endoscopic vitreoretinal surgery: principles, applications and new directions. Int J Retina Vitr. https://doi.org/10.1186/s40942-019-0165-z
3. Li X, Chudoba C, Ko T, Pitris C, Fujimoto JG (2000) Imaging needle for optical coherence tomography. Opt Lett 25(20):1520–1522. https://doi.org/10.1364/OL.25.001520
4. Schoovaerts M, Ourak M, Borghesan G, Putzeys T, Vander Poorten E, Verhaert N (2024) OCT-based intra-cochlear imaging and 3D reconstruction: ex vivo validation of a robotic platform. Int J Comput-Assist Radiol Surg 19(5):917–927. https://doi.org/10.1007/s11548-024-03081-7
5. Balicki M, Han J, Iordachita I, Gehlbach P, Handa J, Taylor R, Kang J (2009) Single fiber optical coherence tomography microsurgical instruments for computer and robot-assisted retinal surgery. In: Medical image computing and computer-assisted intervention-MICCAI 2009, 108–115. https://doi.org/10.1007/978-3-642-04268-3_14
6. Ramakonar H, Quirk BC, Kirk RW, Li J, Jacques A, Lind CRP, McLaughlin RA (2018) Intraoperative detection of blood vessels with an imaging needle during neurosurgery in humans. Sci Adv. https://doi.org/10.1126/sciadv.aav4992
7. Cereda MG, Parrulli S, Douven Y, Faridpooya K, Romunde S, Hüttmann G, Eixmann T, Schulz-Hildebrandt H, Kronreif G, Beelen M, Smet MD (2021) Clinical evaluation of an instrument-integrated OCT-based distance sensor for robotic vitreoretinal surgery. Ophthalmol Sci. https://doi.org/10.1016/j.xops.2021.100085
8. Briel M, Wu D, Hess M, Haide L, Piccinelli N, Kronreif G, Pellegrini M, Tagliabue E, Mathis-Ullrich F (2026) Distance-based shared control for vitreoretinal surgery. IEEE Robot Autom Lett 11(2):1858–1865. https://doi.org/10.1109/LRA.2025.3641113
9. Song C, Park DY, Gehlbach PL, Park SJ, Kang JU (2013) Fiber-optic OCT sensor guided SMART micro-forceps for microsurgery. Biomed Opt Express 4(7):1045–1050. https://doi.org/10.1364/BOE.4.001045
10. Abid A, Duval R, Rezende F, Boutopoulos C (2021) A smart vitrector equipped by a fiber-based OCT sensor mitigates intentional attempts at creating iatrogenic retinal breaks during vitrectomy in pigs. Transl Vision Sci Technol. https://doi.org/10.1167/tvst.10.13.19
11. Wu D, George KT, Matten P, Tagliabue E, Ataman C (2025) Towards assessment of retinal morphological changes via instrument-integrated OCT in endo-photocoagulation in a porcine eye model. In: European conferences on biomedical optics 2025, pp. 1–5 . https://doi.org/10.1364/ECBO.2025.S1B.5
12. Lauermann P, Klingelhöfer A, Mielke D, Oterendorp C, Hoerauf H, Striebe N-A, Storch MW, Pfeiffer S, Koscielny J, Sucker C, Bemme S, Feltgen N (2021) Risk factors for severe bleeding complications in vitreoretinal surgery and the role of antiplatelet or anticoagulant agents. Ophthalmol Retina 5(8):23–29. https://doi.org/10.1016/j.oret.2021.04.013
13. Bergamo VC, Caiado RR, Maia A, Magalhães O, Moraes NSB, Rodrigues EB, Farah ME, Maia M (2021) Role of vital dyes in chromovitrectomy. Asia-Pacific J Ophthalmol 10(1):26–38. https://doi.org/10.1097/APO.0000000000000344
14. Mohr A, Cendoya P, Wilinska J, Apostu M, Apostu E, Janku J, Wilfling T, Ramos G, Al-Joumhawy M, Gabel D (2022) New dual dye for vitreoretinal surgery with increased transparency. BMJ Open Ophthalmol. https://doi.org/10.1136/bmjophth-2022-001116

15. Williamson TH (2021) Introduction to vitreoretinal surgery 1, pp. 23–62. Springer, Cham. https://doi.org/10.1007/978-3-030-68769-4_2
16. Aasuri M, Kompella V, Majji A (2001) Risk factors for and management of dropped nucleus during phacoemulsification. J Cataract Refract Surg 27(9):1428–1432. https://doi.org/10.1016/s0886-3350(01)00784-2
17. Lee S, Kang JU (2021) CNN-based CP-OCT sensor integrated with a subretinal injector for retinal boundary tracking and injection guidance. J Biomed Optics. https://doi.org/10.1117/1.JBO.26.6.068001
18. Bazvand F, Ghassemi F (2020) Artifacts in macular optical coherence tomography. J Curr Ophthalmol 32(2):123–131. https://doi.org/10.4103/JOCO.JOCO_83_20
19. Braaf B, Vermeer KA, Groot M, Vienola KV, Boer JF (2014) Fiber-based polarization-sensitive OCT of the human retina with correction of system polarization distortions. Biomed Opt Express 5(8):2736–2758. https://doi.org/10.1364/BOE.5.002736
20. Briel M, Haide L, Hess M, Schimmelpfennig J, Matten P, Peter R, Hillenbrand M, Tagliabue E, Mathis-Ullrich F (2025) Intraoperative adaptive eye model based on instrument-integrated OCT for robot-assisted vitreoretinal surgery. Int J Comput Assist Radiol Surg. https://doi.org/10.1007/s11548-025-03325-0
21. Acheson RW, Capon M, Cooling RJ, Leaver PK, Marshall J, McLeod D (1987) Intraocular argon laser photocoagulation. Eye 1, 97–105 https://doi.org/10.1038/eye.1987.15
22. Cornelissen P, Ourak M, Borghesan G, Reynaerts D, Poorten EV (2019) Towards real-time estimation of a spherical eye model based on a single fiber OCT. In: 2019 19th International conference on advanced robotics (ICAR), pp. 666–672. https://doi.org/10.1109/ICAR46387.2019.8981620
23. Briel M, Haide L, Emmrich J, Piccinelli N, Kronreif G, Tagliabue E, Mathis-Ullrich F (2025) Intraoperative 3D reconstruction and geometric modeling using sensorized microsurgical instruments. IEEE Trans Med Robot Bionics. https://doi.org/10.1109/TMRB.2025.3604119
24. Jungo A, Doorenbos L, Col TD, Beelen M, Zinkernagel M, Márquez-Neila P, Sznitman R (2023) Unsupervised out-of-distribution detection for safer robotically guided retinal microsurgery. Int J Comput Assist Radiol Surg 18(6):1085–1091. https://doi.org/10.1007/s11548-023-02909-y
25. Piccinelli N, Haide L, Briel M, Jungo A, Tagliabue E, Da Col T, Schmid M, Sznitman R, Pellegrini M, Yu AC, Busin M, Mura M, Muradore R, Kronreif G (2025) GEYEDANCE: an OCT-enhanced multi-modal feedback platform for robot-assisted ophthalmic surgery. IEEE Trans Med Robot Bionics. https://doi.org/10.1109/TMRB.2025.3583133
26. Sifferman C, Mehrotra D, Gupta M, Gleicher M (2022) Geometric calibration of single-pixel distance sensors. IEEE Robot Autom Lett 7(3):6598–6605. https://doi.org/10.1109/LRA.2022.3176453
27. Briel M, Haide L, Meyling M, Saalfrank B, Matten P, Piccinelli N, Kronreif G, Spadea F, Tagliabue E, Mathis-Ullrich F (2025) Curvature-corrected retinal registration of diagnostic OCT with instrument-integrated OCT. Sci Rep 15(1):42933. https://doi.org/10.1038/s41598-025-28922-6
28. Kinkelder R, Kalkman J, Faber DJ, Schraa O, Kok PHB, Verbraak FD, Leeuwen TG (2011) Heartbeat-induced axial motion artifacts in optical coherence tomography measurements of the retina. Investig Ophthalmol Vis Sci 52(6):3908–3913. https://doi.org/10.1167/iovs.10-6738
29. Arikan D, Esfandiari M, Zhang P, Sommersperger M, Dehghani S, Taylor RH, Nasseri MA, Gehlbach P, Navab N, Iordachita I (2025) Towards motion compensation in autonomous robotic subretinal injections. In: 2025 International symposium on medical robotics (ISMR), pp. 66–72. https://doi.org/10.1109/ISMR67322.2025.11025990
30. Braun D, Yang S, Martel JN, Riviere CN, Becker BC (2018) EyeSLAM: Real-time simultaneous localization and mapping of retinal vessels during intraocular microsurgery. The Int J Med Robot Comput Assist Surg 14(1):1848. https://doi.org/10.1002/rcs.1848
31. Liu P, Golde J, Morgenstern J, Bodenstedt S, Li C, Hu Y, Chen Z, Koch E, Neudert M, Speidel S (2024) Non-rigid point cloud registration for middle ear diagnostics with endoscopic optical coherence tomography. Int J Comput Assist Radiol Surg. https://doi.org/10.1007/s11548-023-02960-9